Aerodynamic Matching Optimization of the Second-Stage Stator of Centrifugal Compressor

Qinglong Liu , Hang Lv , Lingang Shen , Xiaofang Wang , Haitao Liu *

Posted Date: 3 March 2026

doi: 10.20944/preprints202603.0122.v1

Keywords: centrifugal compressor; second-stage stator; parametric modeling; CFD; kriging; genetic algorithm; multi-objective optimization

 doi:10.20944/preprints202603.0122.v1

Article

Aerodynamic Matching Optimization of the Second-Stage Stator of Centrifugal Compressor

Qinglong Liu [1,2], Hang Lv [1], Lingang Shen [2], Xiaofang Wang [1], Haitao Liu [1,*]

[1] School of Energy and Power Engineering, Dalian University of Technology, Dalian, Liaoning, China, 110624
[2] Hangzhou Chinen Turbomachinery Co., Ltd., Hangzhou, Zhejiang, China, 311228
* Correspondence: htliu@dlut.edu.cn

Abstract

This paper presents a parametric modeling and aerodynamic optimization methodology for the second-stage stator of a multi-stage centrifugal compressor. Based on the geometric configuration of the two-stage components, a flexible parametric template is established for the second-stage stator. Numerical simulations are conducted to analyze the internal flow field and evaluate the performance of the initial design of this compressor, revealing performance deficits such as significant vortex-induced losses and a large outlet circumferential flow angle (-12.138°). To this end, an aerodynamic optimization framework integrating a Kriging surrogate model and a Genetic Algorithm (GA) is applied to the second-stage stator, targeting at the aerodynamic matching optimization under multiple operating conditions. The optimization objectives include maximizing the overall polytropic efficiency of compressor and static pressure ratio of second-stage stator, as well as minimizing the total pressure loss coefficient and the outlet circumferential flow angle of second-stage stator. The results demonstrate that the optimized design achieves a 2.17% improvement in the overall polytropic efficiency and a 12.01% improvement in the static pressure recovery coefficient at the design condition, along with a notable reduction in the outlet circumferential flow angle to 0.663°. Under multi-condition operation, the optimized stator exhibits enhanced the performance stability. The overall polytropic efficiency is improved by 2.06% and the static pressure recovery coefficient is improved by 23.31% at the low-flow condition, confirming the effectiveness of the proposed parametric modeling and sequential optimization approach.

Keywords: centrifugal compressor; second-stage stator; parametric modeling; CFD; kriging; genetic algorithm; multi-objective optimization

1. Introduction

Centrifugal compressors are often regarded as the "heart" of industrial processes. They are critical equipment in sectors vital to the national economy, including refrigeration, oil refining, petrochemicals, gas separation, metallurgy, and natural gas transmission [1]. They function by leveraging the interaction between the impeller and the gas to increase pressure while imparting kinetic energy to the fluid. Subsequently, the gas decelerates through the stationary components downstream of the impeller, primarily the diffuser and the return channel. Here, kinetic energy is converted into pressure energy, thereby further enhancing the static pressure of the gas [2].

As a critical element for energy conversion in centrifugal compressors, the stator components, e.g., the diffuser, inherently incurs energy losses. Taking a single-stage centrifugal compressor as an example, the expected overall efficiency of domestically designed machines in China is approximately 83%, whereas studies indicate that impeller efficiency can exceed 90% [1]. This discrepancy suggests that energy losses in the stationary components can reduce stage efficiency by as much as 7%, representing a significant portion of the total energy loss. In multi-stage centrifugal compressors, the bend and return channel redirect the flow from the diffuser to the inlet of the next impeller. The losses in

 doi:10.20944/preprints202603.0122.v1

these stationary components are considerable, potentially accounting for 6%–8% of the stage energy. Furthermore, the flow quality at the outlet of the return channel directly impacts the performance of the subsequent impeller [2]. With increasing demands for energy efficiency, research focus has gradually shifted toward stationary components to explore potential energy-saving opportunities and improve overall operational stability.

As a representative stator component, the diffuser, located downstream of the impeller, functions primarily to decelerate the high-velocity airflow and convert kinetic energy into pressure energy. Based on the presence of vanes, As a representative stator component, the diffusers are categorized into vaneless and vaned types. Due to their structural simplicity, research on vaneless diffusers typically focuses on flow field characteristics. As the flow rate decreases, the recirculation zone gradually expands from the hub side to the shroud side, eventually appearing on both walls [3]. Under unstable operating conditions, aerodynamic losses in vaneless diffusers increase significantly, potentially accounting for 33% to 45% of the total machine loss [4]. In contrast, while vaned diffusers can offer higher efficiency, vane-induced losses, such as incidence loss, wake loss, and throat effects, can weak the compressor performance. Studies indicate that the jet-wake structure from the impeller outlet enters into the diffuser without fully mixing. This leads to highly distorted flow angles at the vane leading edge and triggers strong stall phenomena [5]. Furthermore, the impeller wake causes low-energy fluid to accumulate on the diffuser suction surface, while the impeller tip leakage vortex induces unsteady disturbances within the diffuser [6,7]. The unsteady flow characteristics of the diffuser are primarily determined by the flow angle at the vane leading edge. Losses mainly originate from the vortex generation and shedding processes [8]. These unsteady phenomena stem from the interaction between the impeller tip leakage vortex and the diffuser hub corner separation vortex [9]. Additionally, the radial gap between the impeller and diffuser influences both the pressure recovery capability and internal flow separation [6,7,10]. Recent numerical investigations have further quantified this effect, revealing that optimizing the radial gap ratio (specifically increasing it within the range of 1.06 to 1.14) significantly suppresses low-velocity zones at the impeller outlet, thereby enhancing flow uniformity and intake conditions at the diffuser inlet [11].

Compared to the diffuser, the return channel possesses a more complex configuration, comprising a U-bend, a Return Guide Vane (RGV), and an L-bend. Its primary functions are to eliminate residual swirl and guide the flow to the inlet of the next stage [12]. The significant flow turning, exceeding 270°, makes the internal flow exceedingly complex, resulting in losses that far exceed those of the diffuser. Non-uniform flow from the vaneless diffuser is intensified within the U-bend, making the L-bend more prone to flow separation [13]. Reducing flow non-uniformity at the inlet of the return guide vanes is crucial for improving return channel efficiency [14]. This has prompted research specifically focused on the U-bend. Studies have shown that reducing the ratio of the U-bend outlet width to the mean streamline radius of curvature (b/r) can decrease losses and improve flow uniformity at the RGV inlet [15]. Similarly, recent research employing adjoint-based optimization has demonstrated that refining the meridional profile of the return channel—specifically the hub-to-shroud distribution—can significantly reduce entropy generation. Experimental verification confirmed that such geometric optimization yields a consistent stage efficiency improvement of up to 2% across the entire operating range [16].

RGV, while structurally similar to a vaned diffuser, serves a distinct function that necessitates specific design methodologies. Simon et al. [17,18] proposed two meridional flow path designs based on flow area variation. They concluded that a scheme combining simultaneous deceleration and turning in the first half yielded lower losses under most incidence angles. Bisping et al. [19] further emphasized that an appropriate deceleration process within the RGV is critical for efficiency enhancement. Due to its unique function, the RGV design diverges from conventional diffuser vane design. Toyokura et al. [20] introduced an inverse design principle, resulting in cylindrical vanes with a prescribed velocity distribution. Japikse [21] designed two vane types using a method based on the linear reduction of circumferential velocity and circulation. While this improved the outlet flow

 doi:10.20944/preprints202603.0122.v1

field, it also generated secondary flows. Loading control is another prevalent technique. Aungier [22] proposed a widely adopted method based on the distribution of a blade loading parameter. Veress [23] combined the constant loading method with inverse design to develop a three-dimensional RGV. This method effectively suppressed the flow separation and reduced the secondary flows by adjusting the vane lean angle.

In recent years, data-driven optimization has been widely applied in improving the performance of stators and rotors of centrifugal compressor[24]. In the realm of engineering optimization, artificial intelligence (AI) and machine learning (ML) techniques are increasingly applied. Ma et al. [25] developed a novel framework integrating a data-driven surrogate model with a stochastic optimization algorithm for the multi-objective optimization of a centrifugal compressor impeller. It was found that the particle swarm optimization (PSO) was most effective in obtaining the global optimum. It improved the stall margin of a centrifugal compressor with a ring cavity by 1.87%. Bashiri et al. [26] optimized a centrifugal pump impeller using an evolutionary algorithm based on a modified artificial neural network (ANN), PSO, and validated CFD data. Leveraging similar approaches, Zhang et al. [27] combined a genetic algorithm with data mining to optimize the aerodynamic performance under various parameters. Deng et al. [28] employed CFD as a high-fidelity model and support vector machine (SVM) as a surrogate model, coupled with the NSGA-II algorithm, to optimize guide vanes. Zhang et al. [29] integrated CFD, NSGA-II, and an ANN to optimize a helicon-axial multiphase pump, achieving a 10% increase in pressure rise and a 3% improvement in efficiency. Besides, to reduce the computational cost of constructing surrogate models without sacrificing accuracy, Liu et al. [30] proposed a multi-fidelity surrogate model based on flow field extraction (FFMFS). This model, trained on samples of varying fidelity, successfully optimized a 1.5-stage subsonic axial compressor. Finally, Mojaddam and Pullen [31] constructed surrogate models within a design space created using the Box-Behnken method. Their design of experiment (DoE) approach highlighted the most influential factors. , and delivered a design with improvements of 3% in efficiency and 11% in pressure ratio. Most recently, to further address the challenge of high time consumption in high-dimensional optimization, Liu et al. [32] proposed an efficient bionic evolutionary algorithm based on a multi-surrogate model (MMOA-SF). By integrating a sigmoid-based model management strategy and a penalty mechanism for infeasible solutions, this method achieved significant performance gains. Application to a centrifugal impeller showed that the isentropic efficiency and mass flow rate were increased by 1.9% and 4.61% respectively, while the computational cost was reduced by 54.9% compared to traditional meta-heuristic algorithms.

Although extensive research has been conducted on the design and optimization of stationary components, they typically focus on optimizing individual components separately, such as the diffuser or return channel. Additionally, many optimization efforts are conducted exclusively at the design point. This may result in performance degradation under off-design conditions, thereby compromising operational stability. To this end, this paper overlooks a system-level analysis of global parameters across the entire second-stage stators of compressor assembly, and it aims to develop an integrated design and multi-condition optimization framework for the second-stage stationary components of a multi-stage compressor.

2. Parametric Modeling and Simulation of Two-Stage Centrifugal Compressor

This chapter focuses on the CFD simulation and parametric modeling of the second-stage stationary components for the air compressor model illustrated in Figure 1.

 doi:10.20944/preprints202603.0122.v1

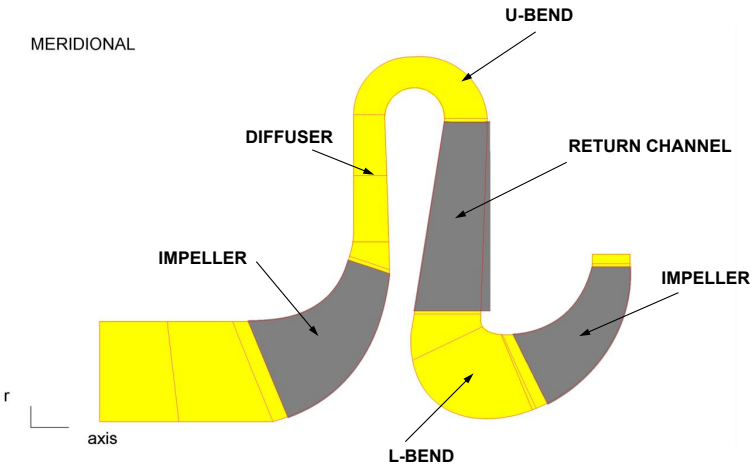

Figure 1. The Meridional View of Multi-stage Air Compressor Model

The research subject comprises a high-flow air compressor assembly, specifically including the first-stage components (impeller, diffuser, bend, and return channel) and the second-stage impeller. The impellers are shrouded and designed for a mass flow rate of 15.7 kg/s at a rotational speed of 9199 rpm, operating with a blade tip Mach number of 0.85. The entire compressor assembly achieves an overall static pressure ratio of 2.5. The first stage employs a vaneless diffuser, while the return channel is designed with straight vanes.

2.1. Initial Design and Parametric Modeling of the Second-Stage Stators

The second-stage stationary components are initially designed to maintain the geometric consistency with those of the first stage. The corresponding initial design parameters are listed in Table 1. Schematic diagrams of the meridional plane and the Blade-to-Blade (B2B) view are presented in Figure 5.

As the inner and outer walls of the first-stage components feature standard semi-circular profiles, the inner wall radius of the bend is defined as a variable parameter in the second-stage parametric model. The geometry of the outer wall is derived from the diffuser outlet width, the bend inner radius, and the return channel inlet width. In contrast, the diffuser inlet and the L-bend outlet are constrained by the dimensions of the adjacent impellers. Consequently, they are treated as fixed parameters. The outer profile of the L-bend is constructed using a composite Bezier curve. This parametric methodology is illustrated in Figure 2, where the curve is defined by three control points.

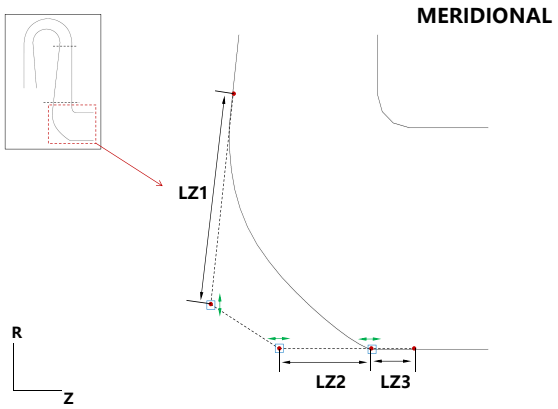

Figure 2. Parametric Second-Stage L-Shaped Bend Based on a Composite Bezier Curve

 doi:10.20944/preprints202603.0122.v1

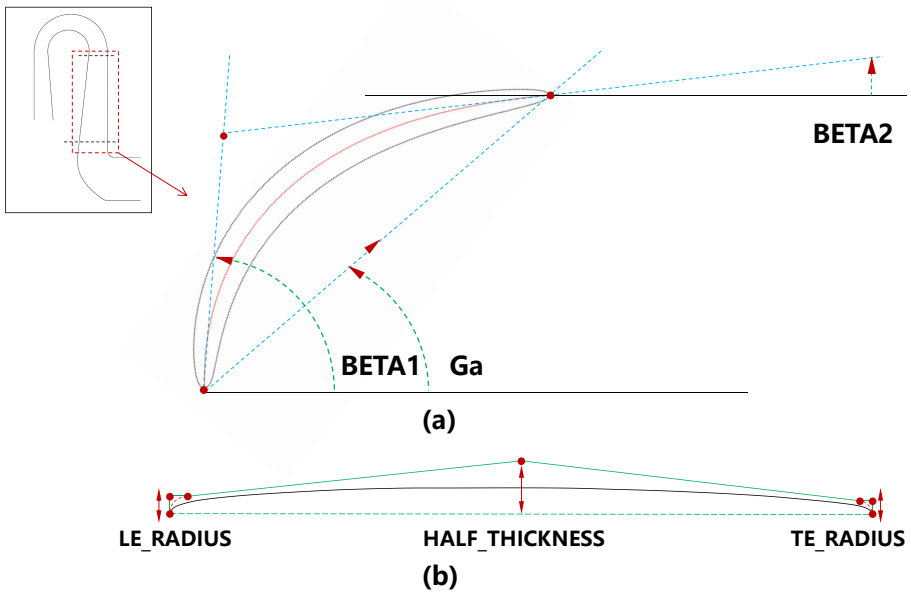

Figure 3. Parametric (a) Mean Camber Line and (b) Blade Thickness Distribution for the Second-Stage Return Channel Blade

Table 1. Initial Design Parameters of the Second-Stage Stators

Parameter	Value (Unit)
Diffuser Inlet Width (B2)	45.6 mm
Diffuser Outlet Width (B4)	37.5 mm
Diffuser Inlet Diameter (D2)	600 mm
Diffuser Outlet Diameter (D4)	1264 mm
Bend Inner Wall Radius (R5)	36 mm
Return Channel Inlet Width (B6)	52 mm
Return Channel Divergence Angle (B7)	9 °
Diameter at Upper Wall of L-Bend (D8)	344 mm
L-Bend Outlet Width (B8)	104 mm
L-Bend Fillet Radius (R9)	5 mm
L-Bend: Composite Bezier Curve Fit Point 1 (LZ1)	85 mm
L-Bend: Composite Bezier Curve Fit Point 2 (LZ2)	2 mm
L-Bend: Composite Bezier Curve Fit Point 3 (LZ3)	19.65 mm
Return Channel Vane Inlet Angle (BETA1)	56 °
Return Channel Vane Outlet Angle (BETA2)	8 °
Return Channel Vane Stagger Angle (Ga)	23 °
Number of Vanes (n)	19
Leading Edge Radius Thickness (LE_RADIUS)	7 mm
Midspan Thickness (HALF_THICKNESS)	20 mm
Trailing Edge Radius Thickness (TE_RADIUS)	5 mm

Additionally, the parametric model for the mean camber line of the second-stage return channel blade is established as illustrated in Figure 3. The parametric model of the flow channel for the second-stage stationary components is depicted in Figure 4.

2.2. CFD Simulation Analysis

Numerical simulations were performed on the initial design of the two-stage centrifugal compressor using the NUMECA software suite. The computational domain encompasses the entire flow path,

 doi:10.20944/preprints202603.0122.v1

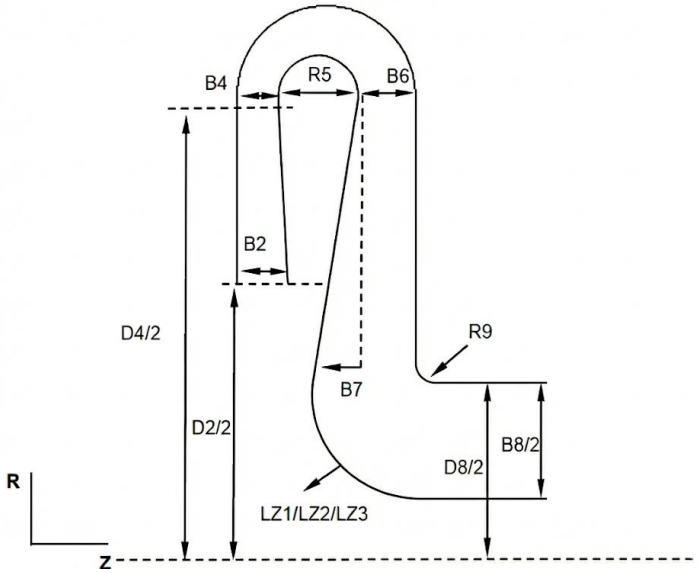

Figure 4. The Overall Parametric Second-Stage Stators

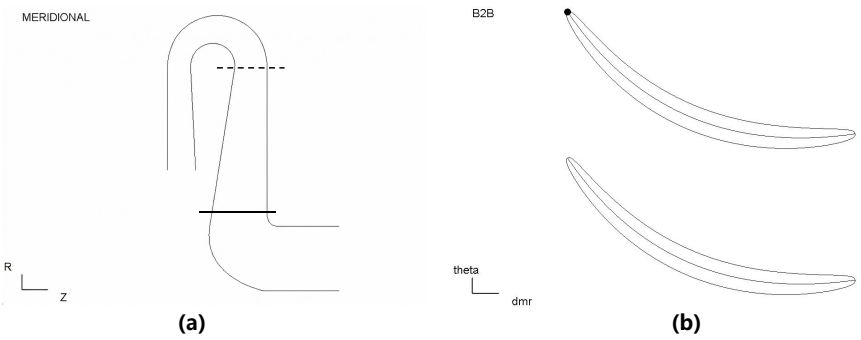

Figure 5. Initial Design of the Second-Stage Stators with (a) the Meridional View and (b) the Blade-to-Blade View of Return Channel Blade

 doi:10.20944/preprints202603.0122.v1

including the first-stage impeller (K1), diffuser, U-bend, return channel, L-bend, and the second-stage impeller (K2), followed by the adapted stators.

The computational mesh was generated within the AutoGrid5 module of NUMECA, resulting in a total grid of approximately 8.92 million cells. This comprises about 1.96 million cells for the first-stage impeller. The first-stage stators account for 2.53 million cells. The second-stage impeller utilizes 2.10 million cells. The adapted stators comprise 2.33 million cells. As shown in Figure 6, the mesh is structured and employs a single-passage model of the computational domain. The grid quality satisfies the requirements for multigrid solvers in the circumferential, spanwise, and streamwise directions. Acceptable aspect ratios, expansion ratios, and minimum orthogonal angles were maintained according to the NUMECA solver standards. A grid independence study was conducted to verify that the chosen mesh density is sufficient. Besides, the Spalart-Allmaras (S-A) turbulence model was selected for the calculations. To ensure a y^+ value of less than 5, the height of the first grid layer adjacent to the wall was set to 0.003 mm. Furthermore, extended inlet and outlet sections were appended to the inlet of the first-stage impeller and the outlet of the second-stage stators, respectively. This ensures the accurate capture of inflow and outflow conditions under realistic flow scenarios.

Figure 6. Single-Passage Computational Mesh of the Centrifugal Compressor

Both the first and second-stage impellers were set to a rotational speed of 9199 rpm. Under the design mass flow condition, the inlet boundary was defined by total temperature, total pressure, and flow direction. The outlet was specified by a mass flow boundary condition. The boundary condition settings are summarized in Table 2.

Table 2. Boundary Condition Settings for Simulation of the Two-Stage Compressor

Boundary Condition	Value (Unit)
Inlet Total Pressure	101350 Pa
Inlet Total Temperature	288.15 K
Inflow Direction	Axial
Design Mass Flow	15.7 kg/s

Numerical calculations were executed using the aforementioned mesh and boundary conditions. The convergence criteria were established as follows. The global residuals were required to drop below 1×10^{-6}. The mass flow conservation error between the inlet and outlet had to be within 0.5%. Additionally, all monitored performance indicators were required to stabilize.

2.3. Performance Evaluation and Flow Analysis

The static pressure recovery coefficient (C_p) and the total pressure loss coefficient (K_p) are adopted as key metrics to evaluate the aerodynamic performance of the stators. They are defined respectively as:

 doi:10.20944/preprints202603.0122.v1

$$C_P = \frac{\overline{P_{out}} - \overline{P_{in}}}{\overline{P_{in}^*} - \overline{P_{in}}} \tag{1}$$

$$K_p = \frac{\overline{P_{in}^*} - \overline{P_{out}^*}}{\overline{P_{in}^*} - \overline{P_{in}}} \tag{2}$$

where:

- $\overline{P_{in}}$ is the average static pressure at the inlet of the stators;
- $\overline{P_{out}}$ is the average static pressure at the outlet of the stators;
- $\overline{P_{in}^*}$ is the average total pressure at the inlet of the stators;
- $\overline{P_{out}^*}$ is the average total pressure at the outlet of the stators.

The coefficient C_p characterizes the capability of converting the kinetic energy into pressure energy. It is defined as the ratio of the static pressure rise to the inlet dynamic pressure, reflecting the pressure recovery capability. Conversely, the coefficient K_p quantifies the total pressure loss relative to the inlet dynamic pressure. This indicates the magnitude of irreversible flow losses within the component.

Numerical simulations of the initial design of two-stage centrifugal compressorwere conducted at the design mass flow rate to obtain the performance parameters and the flow field data. Figure 7 displays the meridional streamlines and the Blade-to-Blade (B2B) flow field at 50% spanfor the second-stage stators. Table 3 summarizes the key performance indicators of the compressor.

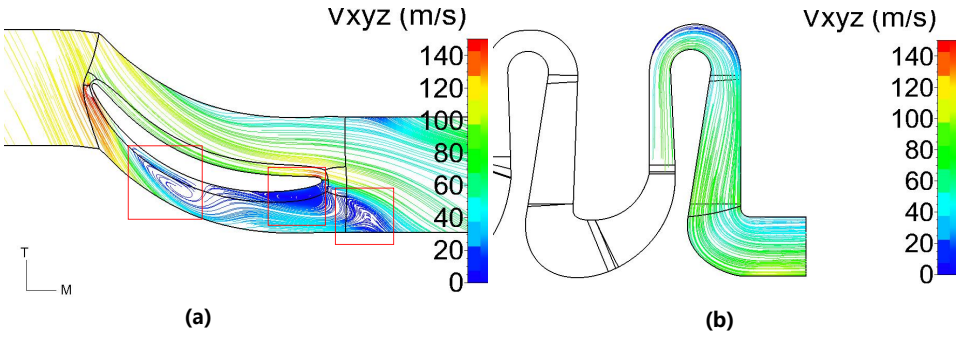

Figure 7. Absolute Velocity Field of the Initial Design of Two-Stage Stators at Design Flow Condition with (a) the B2B View at 50% Span and (b) the Meridional View

Table 3. Key Performance Indicators of the Initial Design of Two-Stage Compressor at Design Flow Condition

Performance Metric	Value (Unit)
Overall Polytropic Efficiency	0.8808
Overall Static Pressure Ratio	2.7394
Outlet Circumferential Flow Angle	-12.138 °
Total Pressure Loss Coefficient (Second-Stage Stators)	0.2008
Static Pressure Recovery Coefficient (Second-Stage Stators)	0.6504

It is found that the flow within the second-stage diffuser and U-bend of the initial design appears smooth. However, within the return channel, three distinct low-velocity vortex regions are identified near the blade suction side and in the outlet wake. These vortices are typically associated with significant aerodynamic losses. This leads to an increase in total pressure loss and a reduction in pressure recovery capability. The outlet of these stators leads directly into the subsequent centrifugal impeller. Centrifugal impellers are typically designed for axial inflow. Therefore, the excessively large

 doi:10.20944/preprints202603.0122.v1

negative outlet circumferential flow angle observed in the stator is detrimental to the performance of the downstream impeller. This can cause increased incidence losses in the next stage.

Figure 8 illustrates the static pressure and entropy distributions for the initial design at the design flow condition. This provides further insight into the flow field characteristics. The static pressure contours reveal a gradual pressure recovery along the flow path. Notable pressure gradients occur in the diffuser and return channel regions. However, localized low-pressure zones are observed near the suction side of the return channel vanes. These coincide with the areas where vortex formation was previously identified. These low-pressure zones are indicative of flow separation and energy loss. Furthermore, the entropy distribution highlights the regions of increased entropy, which correspond to the areas of high irreversible losses. Elevated entropy values are particularly prominent in the return channel vane wake and near the outlet. This confirms the presence of significant vortex-induced losses. The combination of low static pressure and high entropy in these regions substantiates that the initial design suffers from substantial flow separation and energy dissipation, particularly in the return channel.

In addition, the CFD simulations were conducted for off-design conditions to further validate the comprehensive performance. Specifically, a high-flow condition (with the mass flow rate of 19 kg/s) and a low-flow condition (with the mass flow rate of 14 kg/s) were selected. The validation results are presented in Figures 9 and 10. Key performance indicators of the initial design at these multi-flow conditions are presented in Table 4.

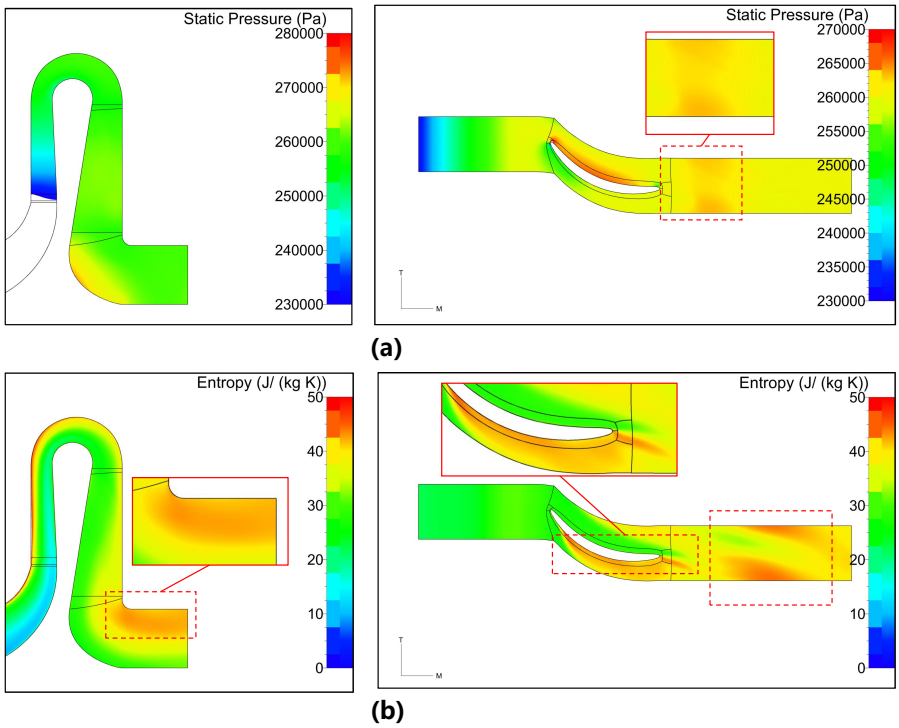

Figure 8. The Meridional View and B2B View (50% Span) of (a) the Static Pressure and (b) the Entropy of the Initial Design at Design Flow Condition

 doi:10.20944/preprints202603.0122.v1

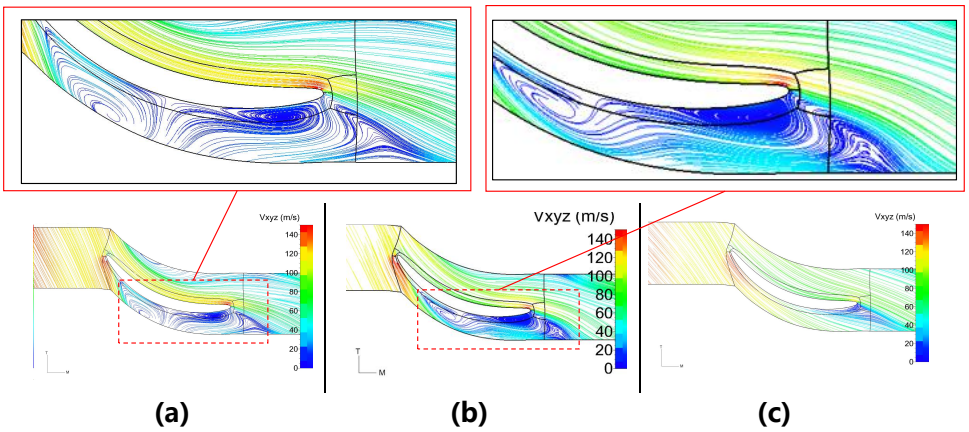

Figure 9. The B2B View (50% Span) of Flow Field of the Initial Design at (a) the Low-Flow Condition, (b) the Designed Flow Condition and (c) the High-Flow Condition

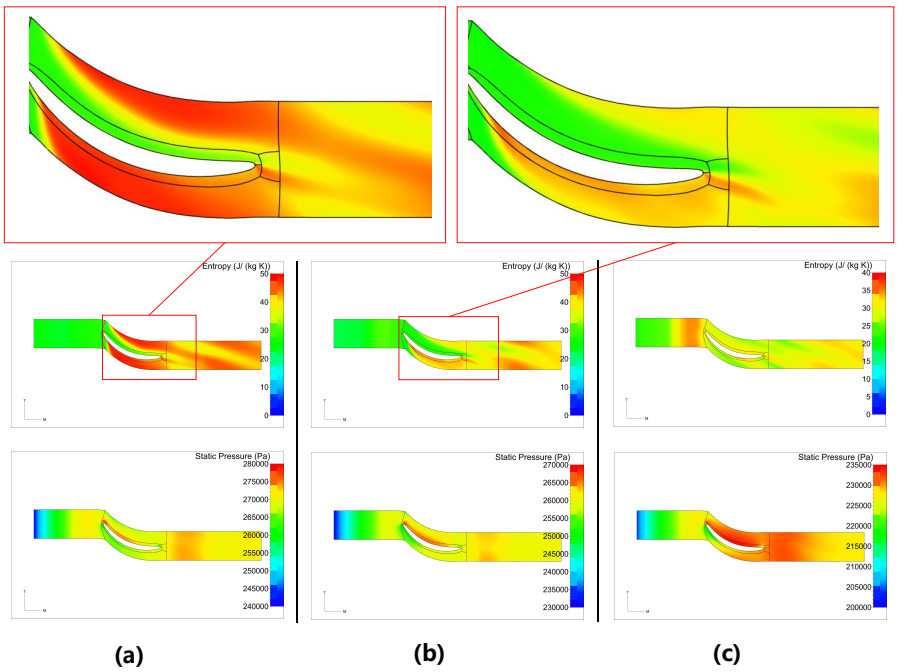

Figure 10. The B2B View (50% Span) of Static Pressure and Entropy of the Initial Design at (a) the Low-Flow Condition, (b) the Designed Flow Condition and (c) the High-Flow Condition

Table 4. Key Performance Indicators of the Initial Design at Different Flow Conditions

Performance Metric	Low-Flow Condition	Design Flow Condition	High-Flow Condition
Overall Polytropic Efficiency	0.8765	0.8808	0.8771
Overall Static Pressure Ratio	2.8097	2.7394	2.4789
Total Pressure Loss Coefficient	0.2839	0.2008	0.1569
Static Pressure Recovery Coefficient	0.6006	0.6504	0.6372

The validation results indicate that the initial design exhibits suboptimal performance across various flow conditions. At the low-flow conditions, the low-velocity vortices within the return channel

 doi:10.20944/preprints202603.0122.v1

persist. This leads to increased total pressure losses and reduced static pressure recovery. The outlet circumferential flow angle remains significantly negative, which is unfavorable for the subsequent impeller stage. In Figure 10, the static pressure and entropy distributions at the low-flow conditions further confirm the existence of flow separation and energy losses in the return channel region. These findings underscore the necessity for optimization to enhance the aerodynamic performance of the second-stage stators.

Consequently, the subsequent optimization aims to mitigate the influence of the low-velocity vortices. It should also reduce the outlet circumferential flow angle as much as possible. The objective is not only to minimize the losses within the current stage but also to create more favorable inflow conditions for the downstream impeller.

3. Aerodynamic Optimization of the Second-Stage Stators

Building upon the established parametric modeling and the CFD simulation framework, this section details the optimization of the second-stage stators.

The general multi-objective optimization problem is mathematically formulated as:

$$\begin{cases} \min F(X) = (f_1(X), f_2(X), \ldots, f_M(X)) \\ s.t.\ g_i(X) \leq 0,\ i = 1, 2, \ldots, l \\ X_{min} \leq X \leq X_{max} \end{cases} \tag{3}$$

where:

- $F(X)$ represents the vector of objective functions to be minimized, with X being the vector of design variables. The optimization targets two primary performance metrics averaged over $M = 3$ operating conditions (low, design, and high mass flow rate). These metrics are the overall polytropic efficiency, $\eta_{p,k}(X)$, and the static pressure ratio, $\Pi_k(X)$, at operating point $k (1 \leq k \leq M)$. They are defined respectively as:

$$\eta_{p,k}(X) = \frac{h^*_{\text{out},k,s}(X) - h^*_{\text{in},k}(X)}{h^*_{\text{out},k}(X) - h^*_{\text{in},k}(X)} \quad \text{for } k = 1, \ldots, M \tag{4}$$

$$\Pi_k(X) = \frac{\overline{P_{\text{out},k}}(X)}{\overline{P_{\text{in},k}}(X)} \quad \text{for } k = 1, \ldots, M \tag{5}$$

Here, h^* denotes the total enthalpy, and the subscripts in, out, and s refer to inlet, outlet, and isentropic conditions, respectively; $\overline{P}$ represents the area-averaged static pressure. To maximize the performance, the objective vector $F(X)$ is defined by minimizing the negative averages of these metrics:

$$F(X) = \Big(-\frac{1}{M}\sum_{k=1}^{M} \eta_{p,k}(X),\ -\frac{1}{M}\sum_{k=1}^{M} \Pi_k(X) \Big) \tag{6}$$

- $g_i(X)$ denotes the set of inequality constraints. These constraints enforce a limit on the outlet circumferential flow angle, α_{out}, at the design point. Additionally, they establish the minimum performance thresholds for efficiency and pressure ratio at each operating point. The constraints are expressed as follows:

 doi:10.20944/preprints202603.0122.v1

$$g_{\alpha}(X) = |\alpha_{\text{out,design}}(X)| - \alpha_{\max} \leq 0 \tag{7}$$

$$g_{\eta,k}(X) = \eta_{p,\min,k} - \eta_{p,k}(X) \leq 0, \qquad k = 1, \ldots, M \tag{8}$$

$$g_{\Pi,k}(X) = \Pi_{\min,k} - \Pi_{k}(X) \leq 0, \qquad k = 1, \ldots, M \tag{9}$$

where, $\alpha_{\max}$ is the maximum allowable flow angle magnitude to ensure near-axial inflow for the downstream impeller; $\eta_{p,\min,k}$ and $\Pi_{\min,k}$ represent the minimum acceptable efficiency and pressure ratio at the operating point k, respectively.

- X_{min} and X_{max} define the lower and upper bounds of the design variables. These boundaries confine the search space to a physically feasible hyper-rectangle, $\mathcal{D}$, ensuring geometric validity as:

$$\mathcal{D} = \{ X \in \mathbb{R}^n \mid X_{\min} \leq X \leq X_{\max} \} \tag{10}$$

3.1. Optimization Strategy

This study develops a CFD-based optimization framework to efficiently enhance the aerodynamic performance of the second-stage stators. The overall methodology integrates the parametric modeling, Design of the DOE technique, the surrogate-assisted optimization, and technique CFD validation. Given the high computational cost associated with direct CFD-based optimization, a surrogate model is employed to approximate the objective functions. This approach drastically reduces the number of required numerical simulations.

The technical route primarily consists of the following key steps:

1. **Sample Database Generation:** The Latin Hypercube Sampling (LHS) method [33] is utilized to generate an initial set of sample points within the design space. The size of this initial database is typically set to ten times the number of design variables. The LHS ensures that the sample points are uniformly distributed, providing excellent space-filling properties for initial model construction.
2. **Surrogate Model Construction and Adaptive Sampling:** A Kriging surrogate model [34] is constructed based on the initial samples. To improve global accuracy, an adaptive sampling strategy is implemented. This strategy identifies regions of high prediction error using the Leave-One-Out (LOO) cross-validation method [35], and it iteratively adds new samples in these regions. The number of adaptively added samples is set to 60% of the initial sample size. This process efficiently refines the surrogate model, focusing computational resources where they are most needed.
3. **Multi-Objective Optimization:** The refined Kriging model serves as a fast-to-evaluate objective function for the optimization process. A Multi-Objective Genetic Algorithm (MOGA) [36] is thereafter employed to search for the Pareto-optimal front. The Tournament selection method is used to handle constraints[37]. The concept of pareto dominance is applied to compare and rank thesolutions.
4. **CFD Validation and Final Selection:** The optimal solutions obtained from the GA optimization on the surrogate model are validated through high-fidelity CFD simulations. The final design is selected from the validated Pareto-optimal solutions based on specific engineering requirements.

In summary, the CFD optimization methodology for the second-stage stators is illustrated in Figure 11.

 doi:10.20944/preprints202603.0122.v1

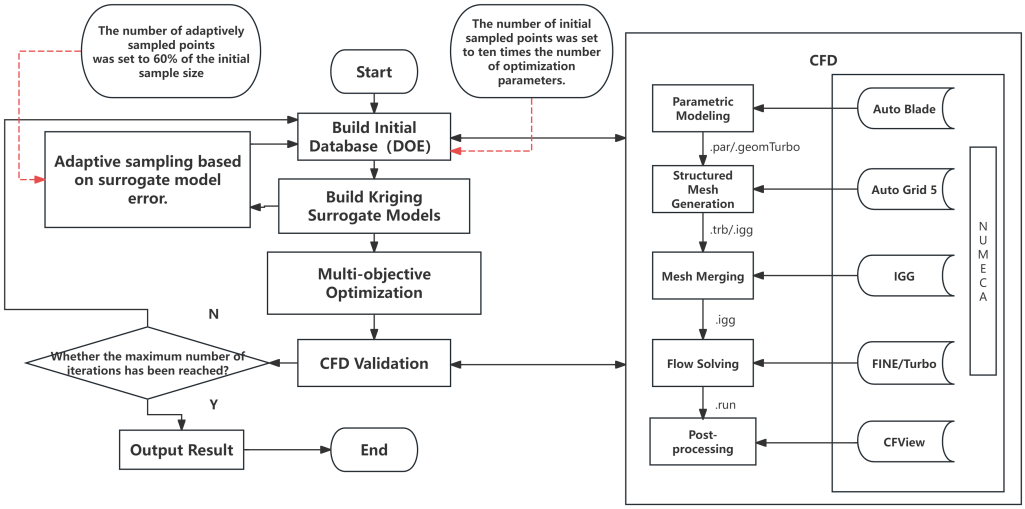

Figure 11. Optimization Methodology for the Second-Stage Stators

The final design is selected based on a comprehensive evaluation of both optimization results and engineering constraints. This integrated methodology significantly reduces the computational costs while ensuring robust, high-performance designs across multiple operating conditions.

3.2. Multi-Point Optimization of Second-Stage Stators

Multi-point optimization was conducted on the second-stage stators. Three representative operating conditions were selected for this process. These are the low-flow condition (mass flow rate of 14 kg/s), the design flow condition (mass flow rate of 15.7 kg/s), and the high-flow condition (mass flow rate of 19 kg/s).

As shown in Table 5, fifteen design variables were selected, which encompass the key geometric features including for example the diffuser outlet width, the bend inner wall radius, the return channel inlet width, the return channel divergence angle, and the L-bend outlet width. Various parameters defining the blade mean camber line and the blade thickness were also included. The objectives were to maximize the average overall polytropic efficiency and the average overall static pressure ratio. Additionally, a constraint was applied to confine the outlet circumferential flow angle at the design flow condition to a narrow range close to zero.

It is notable that as the objectives are average-based, there is a potential risk that optimization could lead to significant performance degradation at a single operating point to improve the overall average. To prevent this, minimum performance thresholds were established as constraints for key indicators at each of the three operating conditions. This resulted in a total of six performance constraints. The definition of this multi-point optimization problem is illustrated in Figure 12, with the design variables and their ranges shown in Table 5.

The optimization process follows a methodology analogous to the single-point optimization. The LHS sampling method was utilized to construct the Kriging surrogate model. The MOGA was subsequently employed to solve the multi-point optimization problem.

 doi:10.20944/preprints202603.0122.v1

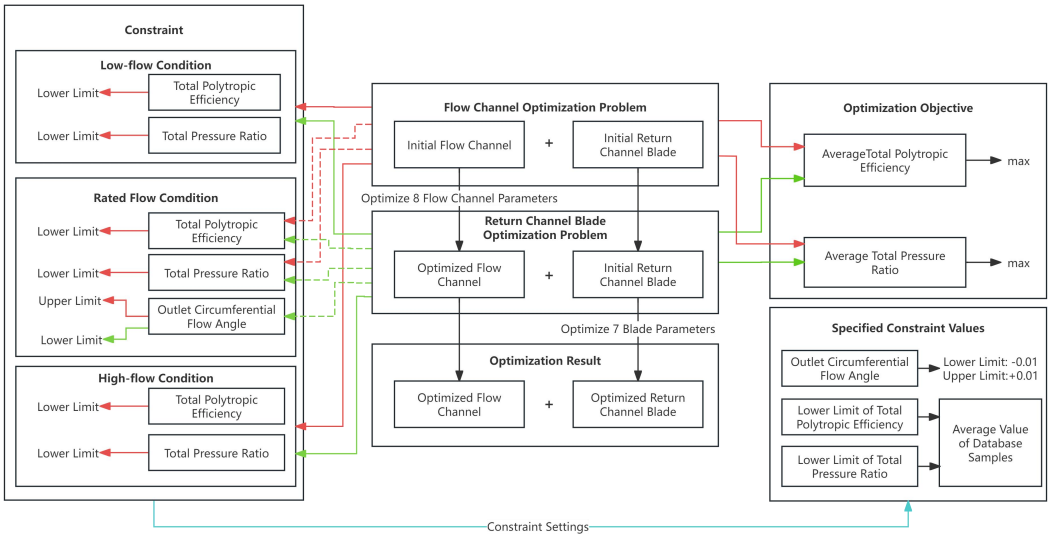

Figure 12. Definition of the Multi-Point Optimization Problem for the Second-Stage Stators

Table 5. Initial Values and Ranges for Design Parameters

Parameter	Upper Bound (Unit)	Lower Bound (Unit)
Diffuser Outlet Width (B4)	27 mm	42.5 mm
Bend Inner Wall Radius (R5)	40 mm	60 mm
Return Channel Inlet Width (B6)	32 mm	50 mm
Return Channel Divergence Angle (B7)	0 °	10 °
L-Bend Fillet Radius (R9)	0 mm	9 mm
L-Bend: Composite Bezier Curve Point 1 (LZ1)	30 mm	100 mm
L-Bend: Composite Bezier Curve Point 2 (LZ2)	2 mm	70 mm
L-Bend: Composite Bezier Curve Point 3 (LZ3)	0.1 mm	25 mm
Return Channel Vane Inlet Angle (BETA1)	47 °	72 °
Return Channel Vane Outlet Angle (BETA2)	0 °	18 °
Return Channel Vane Stagger Angle (Ga)	13 °	25 °
Vane Leading Edge Radius Thickness (LE_RADIUS)	3 mm	12 mm
Vane Midspan Thickness (HALF_THICKNESS)	14 mm	28 mm
Vane Trailing Edge Radius Thickness (TE_RADIUS)	2 mm	8 mm
Number of Vanes (n)	18	28

The optimization involves fifteen design parameters, consisting of eight flow channel parameters and seven vane parameters. To reduce the dimensionality, this optimization problem follows a multi-step strategy, i.e.,, this problem is decomposed into two sub-problems. The first sub-problem focuses on optimizing the eight flow channel parameters. Empirical design experience suggests that the flow channel parameters have limited influence on the outlet circumferential flow angle. Therefore, only the constraints on the overall static pressure ratio and the overall polytropic efficiency at each operating condition were applied to the flow channel optimization. No constraint was imposed on the outlet flow angle for this step. Consequently, the flow channel optimization is formulated as an eight-parameter, two-objective and six-constraint problem. Similarly, for the sub-problem of return channel blade

 doi:10.20944/preprints202603.0122.v1

optimization, the constraints on the overall static pressure ratio and polytropic efficiency were applied. In addition, a constraint on the average outlet circumferential flow angle at the design flow condition was enforced. Thus, the blade optimization is formulated as a seven-parameter, two-objective and eight-constraint problem. The solution strategy follows a sequential approach. The flow channel parameters are optimized first. The resulting optimal flow channel configuration is then used as a fixed basis for the subsequent blade optimization. This process aims to achieve an optimal design for the second-stage stators across multiple flow conditions.

Table 6 presents the performance of the optimized second-stage stators following the multi-point optimization process.

Table 6. Performance Comparison of the Initial and Multi-Point Optimized Designs

Operating Condition	Performance Parameter	Initial Design	Multi-Point Optimized Design
Low-flow Condition	Overall Static Pressure Ratio	2.8097	2.8846
	Overall Polytropic Efficiency	0.8765	0.8946
	Total Pressure Loss Coefficient	0.2839	0.1525
	Static Pressure Recovery Coefficient	0.6006	0.7546
Design-flow Condition	Overall Static Pressure Ratio	2.7394	2.7921
	Overall Polytropic Efficiency	0.8808	0.8999
	Total Pressure Loss Coefficient	0.2008	0.1579
	Static Pressure Recovery Coefficient	0.6504	0.7285
	Outlet Circumferential Flow Angle(°)	-12.138	-0.083767
High-flow Condition	Overall Static Pressure Ratio	2.4789	2.4608
	Overall Polytropic Efficiency	0.8771	0.8727
	Total Pressure Loss Coefficient	0.1569	0.1825
	Static Pressure Recovery Coefficient	0.6372	0.5930

It is found that compared to the initial design of second-stage stators, the multi-point optimized design demonstrates significant performance enhancements across various operating conditions. The improvement is particularly notable under the design flow condition. At the low-flow condition, the overall static pressure ratio is increased by 0.0749. The overall polytropic efficiency is improved by 1.81%. The total pressure loss coefficient is decreased by 0.1314. Meanwhile, the static pressure recovery coefficient is increased by 0.1540. At the design-flow condition, the overall static pressure ratio is increased by 0.0527. The overall polytropic efficiency is improved by 1.91%. The total pressure loss coefficient is decreased by 0.0429. The static pressure recovery coefficient is increased by 0.0781. At the high-flow condition, a slight performance decrement was observed. The overall static pressure ratio is dropped by 0.0181. The overall polytropic efficiency is decreased by 0.44%. However, these losses are minor compared to the substantial gains achieved at low and design flow conditions.

Particularly, a critical improvement is observed for the outlet circumferential flow angle. The value has been improved from an unfavorable -12.138° in the initial design to -0.083° in the optimized design. This near-zero angle indicates that the residual swirl has been effectively eliminated. Consequently, the flow entering the subsequent impeller is almost purely axial. This is essential for minimizing the incidence losses and enhancing the aerodynamic stability of the downstream stage.

 doi:10.20944/preprints202603.0122.v1

Overall, the multi-point optimization has led to substantial performance improvements in most operating conditions. The optimal design has effectively addressed the flow issues identified in the initial design. This has resulted in a more efficient and aerodynamically superior second-stage stators.

3.3. Flow Analysis of Optimized Design

Firstly, a geometric comparison between the initial design and the multi-point optimized design is presented in Figure 13. The optimized design is highlighted in green, and the initial design is marked in blue.

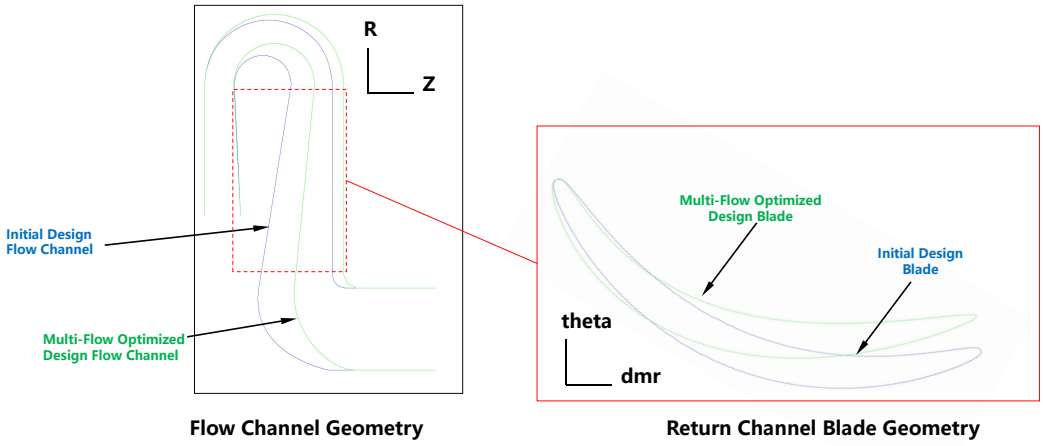

Figure 13. Geometric Comparison Between the Initial Design and Multi-Point Optimized Design

It reveals that the optimized design features a narrower diffuser outlet width and a reduced return channel inlet width. This reduction in flow passage area accelerates the fluid velocity within the channel. It helps to suppress the flow separation and vortex formation, particularly under low-flow conditions. Furthermore, the optimized geometry plays a decisive role in correcting the outlet flow angle. The return channel vanes in the optimized design exhibit a smaller stagger angle and a more moderate inlet angle. These adjustments contribute to improved flow guidance and more effective flow turning. Crucially, the geometric reason for the significant reduction in the outlet circumferential flow angle is the increase in the blade outlet angle. This geometric adjustment effectively reduces the flow deviation angle. It ensures that the flow exits the stators in a nearly axial direction. For the L-bend section, the optimized design features a larger fillet radius and a more gradual curvature. These modifications smooth the flow path, reducing turbulence and energy losses as the fluid navigates the bend.

Secondly, Figure 14 illustrates the velocity streamlines for the initial and optimized designs under low-flow, design-flow, and high-flow conditions. For the initial design, pronounced low-velocity vortex regions are evident near the suction side of the return channel vanes. This is particularly severe at the low-flow condition, indicating significant flow separation and energy dissipation. The multi-point optimized design effectively mitigates the vortex formation across all the three operating conditions. This results in smoother and more uniform streamlines, especially at low flow rates. This demonstrates improved flow stability and reduced aerodynamic losses. The optimized design effectively eliminates the low-velocity vortex regions present in the baseline. This leads to enhanced flow uniformity throughout the stators.

Thirdly, Figure 15 compares the static pressure distributions for the initial and optimized designs at different operating conditions. The initial design exhibits localized regions of low static pressure near the return channel blade suction surfaces and outlet. This corresponds to the areas of flow separation. Differently, the optimized design achieves a more uniform static pressure distribution across all the three conditions. Hence, the low-pressure regions are diminished, indicating enhanced pressure recovery capability.

 doi:10.20944/preprints202603.0122.v1

Finally, Figure 16 displays the entropy distributions for the designs under various flow conditions. The initial design shows elevated entropy values in the wake regions and near the outlet. This reflects high irreversible losses due to the vortex formation. In contrast, the optimized design demonstrates consistently lower entropy across all the three operating conditions. This confirms that the vortex-induced losses and energy dissipation have been effectively suppressed.

In summary, the multi-point optimized design achieves superior flow field characteristics compared to the initial design. It effectively eliminates the low-velocity vortex regions, improves the static pressure recovery, and reduces the entropy generation. This results in enhanced aerodynamic performance and operational stability across the full range of operating conditions.

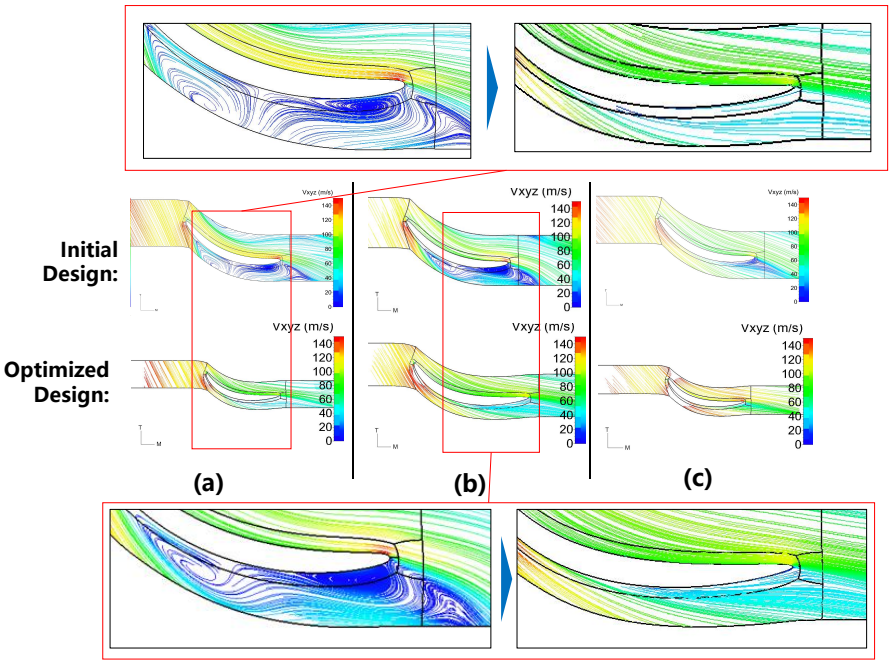

Figure 14. Comparison of the Velocity Streamlines of Initial and Optimized Designs at (a) the Low-flow, (b) the Design-flow, and (c) the High-flow Conditions

 doi:10.20944/preprints202603.0122.v1

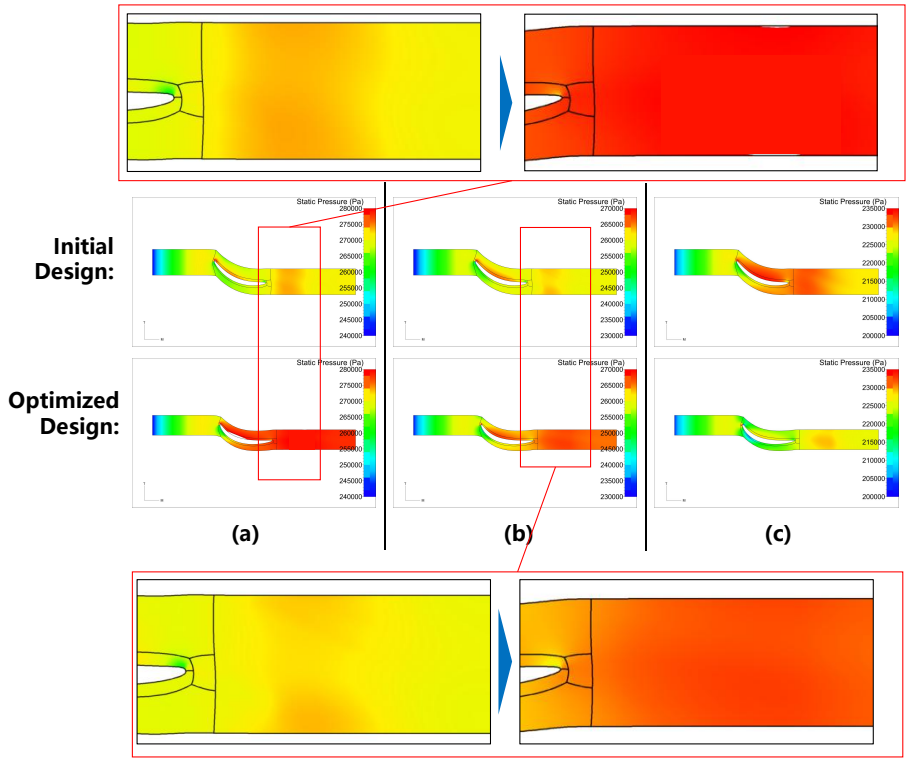

Figure 15. Comparison of Static Pressure Distribution of Initial and Optimized Designs at (a) the Low-flow, (b) the Design-flow, and (c) the High-flow Conditions

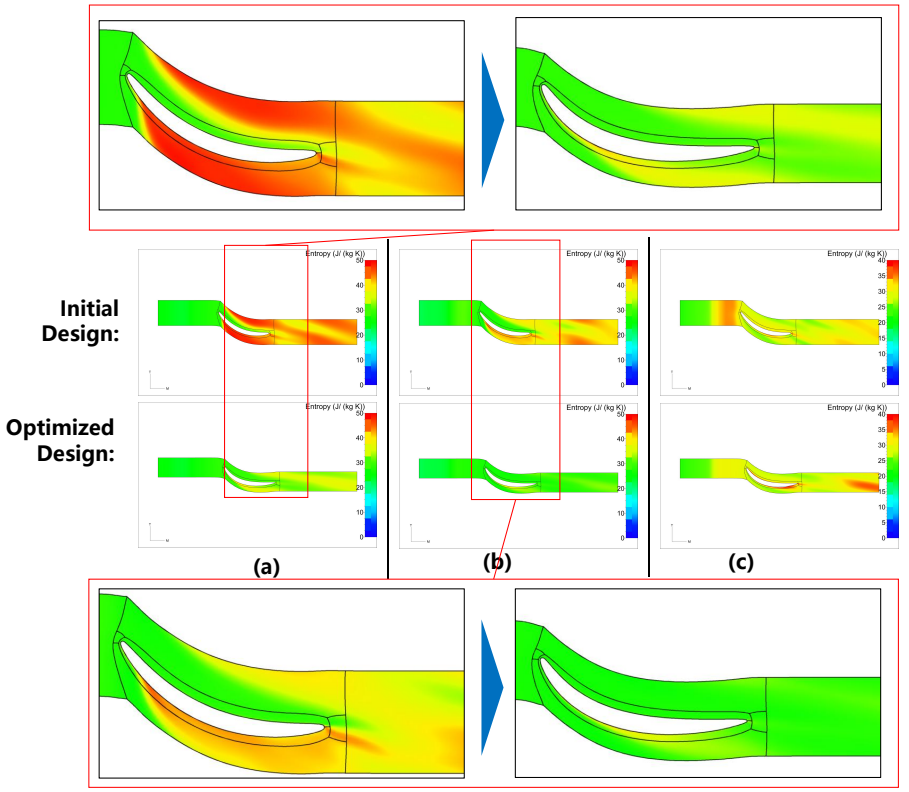

Figure 16. Comparison of Entropy Distribution of Initial and Optimized Designs at (a) the Low-flow, (b) the Design-flow, and (c) the High-flow Conditions

 doi:10.20944/preprints202603.0122.v1

4. Conclusions

This study established a parametric modeling and multi-point aerodynamic matching optimization framework for the second-stage stators of a multi-stage air compressor. The parametric model was constructed based on the geometric configuration of the existing first-stage components to ensure consistency. Utilizing the NUMECA software suite, a comprehensive design workflow was implemented. This encompassed the initial design, the internal flow field simulation, and the aerodynamic optimization. Through a sequential optimization strategy that progressed to a multi-point optimization over three flow rates, a final optimized design was obtained. This optimized design demonstrates excellent performance at the design-flow condition and has robust stability performance under off-design conditions. The results demonstrate that the optimized design achieves a 2.17% improvement in the overall polytropic efficiency and a 12.01% improvement in the static pressure recovery coefficient at the design condition, along with a notable reduction in the outlet circumferential flow angle to 0.663°. Under multi-condition operation, the optimized stator exhibits enhanced performance stability with the overall polytropic efficiency improved by 2.06% and the static pressure recovery coefficient improved by 23.31% at the low-flow condition.

Acknowledgments: This work was supported by the National Natural Science Foundation of China (52375231), the Science and Technology Joint Program of Liaoning Province (2024011954-JH4/4800), the Fundamental Research Funds for the Central Universities (DUT25Z2516), and the Key Research and Development Program of Zhejiang Province (2024C03115).

References

1. Wu C H. A general theory of three-dimensional flow in subsonic and supersonic turbomachines of axial, radial, and mixed-flow types[J]. Transactions of the American Society of Mechanical Engineers, 1952, 74(8): 1363-1380.
2. Veress A, Van den Braembussche R. Inverse design and optimization of a return channel for a multistage centrifugal compressor[J]. J. Fluids Eng., 2004, 126(5): 799-806.
3. Zhang L, Zheng Z, Zhang Q, et al. Study of rotating stall in a centrifugal compressor with wide vaneless diffuser[J]. Journal of Thermal Science, 2020,29:743-752.
4. Shaaban S. Experimental investigation and extended simulation of turbochargernon-adiabatic performance[D]. University of Hanover, 2004.
5. Dawes W N. A Simulation of the Unsteady Interaction of a Centrifugal Impeller With Its Vaned Diffuser:Flow Analysis[J]. Journal of TurbomachineryJournal of Turbomachinery, 1995,117(2):213-222.
6. Boncinelli P, Ermini M, Bartolacci S, et al. Impeller-diffuser interaction in centrifugal compressors:numerical analysis of Radiver test case[J]. Journal of Propulsion and Power, 2007,23(6):1304-1312.
7. Boncinelli P, Ermini M, Bartolacci S, et al. On Effects of Impeller-Diffuser Interaction in the "Radiver" Centrifugal Compressor: ASME Turbo Expo 2007: Power for Land, Sea, and Air[C], 2007.
8. Anish S, Sitaram N, Kim H D. A numerical study of the unsteady interaction effects on diffuser performance in a centrifugal compressor[J]. Journal of Turbomachinery, 2014,136(1):11012.
9. Xue X, Wang T, Shao Y, et al. Experimental and numerical analysis of different unsteady modes in a centrifugal compressor with variable vaned diffuser[J]. Journal of Fluids Engineering, 2019,141(10):101106.
10. Inoue M, Cumpsty N A. Experimental Study of Centrifugal Impeller Discharge Flow in Vaneless and Vaned Diffusers[J]. Journal of Engineering for Gas Turbines and PowerJournal of Engineering for Gas Turbines and Power, 1984,106(2):455-467.
11. Chen J, Zhang Y, Wang Z, et al. Effect of the gap between the diffuser blade and impeller blade on the internal complex flow and aerodynamic performance of a centrifugal compressor[J]. Mechanical Sciences, 2025, 16(2): 549-564.
12. Oh J M, Engeda A, Chung M K. A numerical study of the U-turn bend in return channel systems for multistage centrifugal compressors[J]. Proceedings of the Institution of Mechanical Engineers, Part C: Journal of Mechanical Engineering Science, 2005,219(8):749-756.
13. Brasz J J. Secondary flow in return channels and its effect on multistage compressor performance[C]//Proceedings of the ASME 1998 International Gas Turbine and Aeroengine Congress and Exhibition. Stockholm, Sweden: ASME, 1998: 98-GT-554.

 doi:10.20944/preprints202603.0122.v1

14. Franz H, Rube C, Wedeking M, et al. Numerical investigation of the return channel of a high-flow centrifugal compressor stage: Turbo Expo: Power for Land, Sea, and Air[C], 2015.American Society of Mechanical Engineers.
15. Lenke L J, Simon H. Numerical Investigations on the Optimum Design of Return Channels of MultiStage Centrifugal Compressors: Turbo Expo: Power for Land, Sea, and Air[C], 1999. American Society of Mechanical Engineers.
16. Hanimann L, Fleischli B, Mangani L, et al. Experimentally Verified Optimization of a Two-Stage Real Gas Centrifugal Compressor Using an Industrial-Ready Adjoint Method[J]. Journal of Turbomachinery, 2025, 147(12): 121009.
17. Simon H, Rothstein E. On the development of return passages of multi-stage centrifugal compressors[J]. ASME FED, 1983,3:1-11.
18. Rothstein E. Experimentelle und theoretische Untersuchung der Strömungsvorgänge in Rückführkanälen von Radialverdichterstufen, insbesondere solcher mit geringen Kanalbreiten[M].1984.
19. Bisping J, Jeschke P. Detecting Multidimensional Pareto Fronts During the Optimization of a Return Channel Within a Centrifugal Compressor[J]. Journal of Turbomachinery, 2022,144(4):41003.
20. TOYOKURA T, Kanemoto T, HATTA M. Studies on Circular Cascades for Return Channels of Centrifugal Turbomachinery: 1st Report, Inverse Method and Cascade Design[J]. Bulletin of JSME, 1986,29(255):2885-2892.
21. Japikse, David. Centrifugal compressor design and performance[M]. Centrifugal compressor design and performance, 1988.
22. Aungier R H. Aerodynamic design and analysis of vaneless diffusers and return channels:Turbo Expo:Power for Land, Sea, and Air[C], 1993. American Society of Mechanical Engineers.
23. Veress Á. Computational investigation on deswirl vanes for multistage centrifugal compressors[J]. Periodica Polytechnica Transportation Engineering, 2003,31(1-2):53-78.
24. Anjomrouz A, Zou W, Kong W, et al. Surrogate-assisted Multi-component Aerodynamic Optimization of Centrifugal Compressor Towards Performance Improvement of Adaptive Cycle Engine[J]. Journal of Applied Fluid Mechanics, 2025, 18(12): 2941-2952.
25. Ma, Chongbin, et al. "Multi-objective optimization of the centrifugal compressor impeller in 130 kW PEMFC through coupling SVM with NSGA-III algorithms." International Journal of Green Energy 18.13 (2021): 1383-1395.
26. Bashiri M, Derakhshan S, Shahrabi J. Design optimization of a centrifugal pump using particle swarm optimization algorithm[J]. International Journal of Fluid Machinery and Systems, 2019, 12(4): 322-331.
27. Zhang, Yuemeng, Sichuan Xu, and Yu Wan. "Performance improvement of centrifugal compressors for fuel cell vehicles using the aerodynamic optimization and data mining methods." International Journal of Hydrogen Energy 45.19 (2020): 11276-11286.
28. Deng, Yajun, Bo Yu, and Dongliang Sun. "Multi-objective optimization of guide vanes for axial flow cyclone using CFD, SVM, and NSGA II algorithm." Powder Technology 373 (2020): 637-646.
29. Zhang, Jinya, et al. "Multi-objective shape optimization of helico-axial multiphase pump impeller based on NSGA-II and ANN." Energy Conversion and Management 52.1 (2011): 538-546.
30. Liu Y, Gong W, Li Y, et al. Performance Optimization of an Axial Compressor Using a Novel Multifidelity Surrogate Model Based on Flow Field Extraction[J]. Journal of Engineering for Gas Turbines and Power, 2025, 147(8): 081001.
31. Mojaddam M, Pullen K R. Optimization of a centrifugal compressor using the design of experiment technique[J]. Applied Sciences, 2019, 9(2): 291.
32. Liu J, Liu M, Liu B. An efficient optimization design method for centrifugal compressor blades[J]. Transactions of the Canadian Society for Mechanical Engineering, 2025, 49(3): 459-474.
33. Habibi F I, Hartono F, Prayogo H. Optimization of an annular combustion chamber for micro turbo jet system[C]//IOP Conference Series: Materials Science and Engineering. IOP Publishing, 2019, 645(1): 012009.
34. Gaspar B, Teixeira A P, Soares C G. Assessment of the efficiency of Kriging surrogate models for structural reliability analysis[J]. Probabilistic engineering mechanics, 2014, 37: 24-34.
35. Elisseeff A, Pontil M. Leave-one-out error and stability of learning algorithms with applications[J]. NATO science series sub series iii computer and systems sciences, 2003, 190: 111-130.
36. Coello C A C, Lamont G B. Applications of multi-objective evolutionary algorithms[M]. World Scientific, 2004.

 doi:10.20944/preprints202603.0122.v1

37. Takami H, Obayashi S. A comparator-based constraint handling technique for evolutionary algorithms[J]. AIP Advances, 2022, 12(5).